

Mean-field treatment of the long-range transverse field Ising model with fermionic Gaussian states

Michael P. Kaicher^{1,*}, Davide Vodola^{2,†} and Simon B. Jäger³

¹*Departamento de Física Teórica, Universidad Complutense, 28040 Madrid, Spain*

²*Dipartimento di Fisica e Astronomia, Università di Bologna, I-40129, Bologna, Italy*

³*Department of Physics and Research Center OPTIMAS, University of Kaiserslautern-Landau, D-67663 Kaiserslautern, Germany*



(Received 7 January 2023; revised 11 April 2023; accepted 11 April 2023; published 25 April 2023)

We numerically study the one-dimensional long-range transverse field Ising model (TFIM) in the antiferromagnetic (AFM) regime at zero temperature using generalized Hartree-Fock (GHF) theory. The spin-spin interaction extends to all spins in the lattice and decays as $1/r^\alpha$, where r denotes the distance between two spins and α is a tunable exponent. We map the spin operators to Majorana operators and approximate the ground state of the Hamiltonian with a fermionic Gaussian state (FGS). Using this approximation, we calculate the ground-state energy and the entanglement entropy, which allows us to map the phase diagram for different values of α . In addition, we compute the scaling behavior of the entanglement entropy with the system size to determine the central charge at criticality for the case of $\alpha > 1$. For $\alpha < 1$ we find a logarithmic divergence of the entanglement entropy even far away from the critical point, a feature of systems with long-range interactions. We provide a detailed comparison of our results to outcomes of density matrix renormalization group (DMRG) and the linked cluster expansion (LCE) methods. In particular, we find excellent agreement of GHF with DMRG and LCE in the weak long-range regime $\alpha \geq 1$, and qualitative agreement with DMRG in the strong-long range regime $\alpha \leq 1$. Our results highlight the power of the computationally efficient GHF method in simulating interacting quantum systems.

DOI: [10.1103/PhysRevB.107.165144](https://doi.org/10.1103/PhysRevB.107.165144)

I. INTRODUCTION

Quantum phase transitions describe the behavior of quantum many-body systems at zero temperature when tuning a nonthermal control parameter, such as an applied magnetic field. The phase transition appears as a result of competing phases that describe the ground state at the corresponding parameter and typically lead to a fundamental change in the nature of the correlation present in the ground state. Quantum many-body systems can undergo a quantum phase transition and their study has led to the discovery of many exotic collective phenomena such as superconducting ground states [1], long-range topological order [2], and anyonic statistics [3]. Close to the critical point, the properties of many different physical systems can be classified by a universality class, which is independent of the system size and only depends on the underlying dimensions and symmetries of the problem. In this situation, one can in many instances describe the many-body problem by an interacting spin system [4].

One of the paradigmatic microscopic models displaying a quantum phase transition is the transverse field Ising model (TFIM) at zero temperature [5]. This model is exactly solvable in the limit of short-range, nearest-neighbour interactions. However, the solution of this problem is much harder if one considers beyond nearest-neighbour or even long-range in-

teractions [6–10]. Long-range interacting systems can host exotic states of quantum matter and are therefore of large scientific interest. Recent advances have made effective long-range spin-interactions experimentally accessible [11–15]. In such systems, the effective interaction extends to all spins in the lattice and decays as a power law $1/r^\alpha$, where r is the distance of the spins in the lattice and α is a tunable algebraic exponent. In the experiments one can realize $0 \leq \alpha \leq 3$, which allows one to experimentally probe the regime of long-range interactions in spin systems [11].

In order to analyze the properties of a quantum many-body system, it is important to study large system sizes, which is in our case the number of spins N . The exponential scaling of the Hilbert space dimension with N makes the *ad hoc* diagonalization of such many-body problems illusive. Consequently, one demands numerical methods, which are able to capture the qualitative behavior of the many-body system with a computational cost that displays a low scaling with N . A range of many-body methods of varying computational complexity have been applied to study finite-size long-range quantum many-body systems, including quantum Monte Carlo (QMC) [16], stochastic series expansion QMC [17], a combination of QMC and renormalization group methods [18], Lanczos exact diagonalization [19], and density matrix renormalization group (DMRG) [6,8]. Recently, a method to study short-range quantum-lattice models in the thermodynamic limit, the linked-cluster expansion (LCE), has been extended to allow for the study of long-range systems for $\alpha > 1$ [9,10].

In this paper, we add generalized Hartree-Fock (GHF) theory to this mix of methods. GHF is a *mean-field method*,

*Corresponding author: michael.p.kaicher(at)gmail.com

†Now at: BASF Digital Solutions, Next Generation Computing, Pfalzgrafenstr. 1, D-67056, Ludwigshafen, Germany.

which aims to approximate the ground state of an interacting quantum system as a free electron gas [20], where the latter describes a class of variational functions known as fermionic Gaussian states (FGS). Due to its mean-field nature, GHF is a method with very low computational cost, where the most-demanding compute operation—the evaluation of the Pfaffian $\text{Pf}(\mathbf{A})$ of a $M \times M$ matrix \mathbf{A} —scales at most as $\mathcal{O}(M^3)$ [21]. Even though FGS describe ground or thermal states of quadratic fermionic Hamiltonians [22], they have been applied to various areas of quantum many-body physics with great success, most notably as *ab initio* methods to obtain approximate ground states in electronic structure problems and to condensed matter systems [20,23,24]. In this paper, we demonstrate for the TFIM that GHF achieves qualitatively and quantitatively similar results as non-mean-field methods such as DMRG and LCE, which are designed to describe strongly correlated quantum many-body systems. In order to find the FGS, which best approximates the ground state of the long-range TFIM, we employ two physically-motivated methods, which have been described in Ref. [23]. The first one (ITE) derives the ground state using imaginary time evolution. The second one (ZT) uses a self-consistent equation for the FGS ground-state covariance matrix. Using these two methods we calculate the ground-state energy and the entanglement entropy. By comparison of these results with the ones obtained from DMRG and ZT we will show that GHF is able to capture the qualitative and quantitative behavior of the long-range TFIM. This highlights the ability of GHF in predicting physically relevant material properties at computationally low cost.

This paper is structured as follows. In Sec. II we discuss the GHF theory, which we then apply to the TFIM model described in Sec. II A. The introduced methods are used in Sec. III where we numerically study the ground-state energy and the entanglement entropy. We conclude by summarizing our findings in Sec. IV and providing an outlook for future work.

II. THEORY

A. Long-range transverse field Ising model

In this paper we consider the TFIM Hamiltonian describing a system of N spins with open boundary conditions

$$\hat{H} = \sum_{p=1}^N h_p \hat{\sigma}_p^z + \sum_{p<q}^N J_{pq} \hat{\sigma}_p^x \hat{\sigma}_q^x, \quad (1)$$

where we introduced the transversal magnetic field strength $h_p = \cos(\theta)$, the interaction strength $J_{pq} = \sin(\theta)/|p-q|^\alpha$ and the Pauli matrices $\hat{\sigma}_p^a$ ($a \in \{x, y, z\}$) for each spin indexed by p, q . The magnetic field and interactions strengths are parameterized by the angle θ and the algebraic scaling of the interaction range is given by α . In this paper we furthermore focus on *antiferromagnetic* (AFM) couplings, which implies $J_{pq} > 0$ or $\theta \in (0, \pi)$. Because the Hamiltonian is symmetric under the simultaneous transformations $\hat{\sigma}_p^z \mapsto -\hat{\sigma}_p^z$ and $\theta \rightarrow \pi - \theta$ we can restrict our study to $\theta \in (0, \pi/2]$.

In a next step, we map the TFIM Hamiltonian onto a fermionic Hamiltonian. To this end, we use the Jordan-Wigner transformation $\hat{\sigma}_p^+ = \hat{c}_p^\dagger e^{i\pi \sum_{q=1}^{p-1} \hat{c}_q^\dagger \hat{c}_q}$ and $\hat{\sigma}_p^- = \hat{c}_p e^{-i\pi \sum_{q=1}^{p-1} \hat{c}_q^\dagger \hat{c}_q}$

[25]. Here, we used $\hat{\sigma}_p^\pm = [\hat{\sigma}_p^x \pm i\hat{\sigma}_p^y]/2$ and introduced the fermionic raising and lowering operators $\hat{c}_p^\dagger, \hat{c}_p$, respectively. The latter obey the canonical anticommutation relations $\{\hat{c}_p, \hat{c}_q\} = 0$ and $\{\hat{c}_p, \hat{c}_q^\dagger\} = \delta_{p,q}$, where $\delta_{p,q}$ is the Kronecker delta and $\{\hat{A}, \hat{B}\} = \hat{A}\hat{B} + \hat{B}\hat{A}$ denotes the anticommutator of two operators \hat{A}, \hat{B} . Instead of analyzing the problem in the basis of the $2 \times N$ fermionic operators $\hat{c}_p, \hat{c}_p^\dagger$ we represent the Hamiltonian in $2N$ Majorana operators $\hat{a}_{2p-1} = \hat{c}_p^\dagger + \hat{c}_p$ and $\hat{a}_{2p} = i(\hat{c}_p^\dagger - \hat{c}_p)$. The latter posses the anticommutation relation $\{\hat{a}_l, \hat{a}_m\} = 2\delta_{l,m}$ ($l, m = 1, 2, \dots, 2N$) and the Hamiltonian (1) in the Majorana representation is given by

$$\hat{H} = -i \sum_{p=1}^N h_p \hat{a}_{2p-1} \hat{a}_{2p} + \sum_{p<q}^N (-i)^{q-p} J_{pq} \hat{a}_{2p} \hat{S}_{pq} \hat{a}_{2q-1}. \quad (2)$$

Here, we introduced the string operator $\hat{S}_{pq} = \prod_{k=p+1}^{q-1} (\hat{a}_{2k-1} \hat{a}_{2k})$, which is the product of $2 \times (q-p+1)$ Majorana operators. For nearest-neighbour interactions, $\alpha = \infty$ and $J_{pq} = \delta_{p,q\pm 1}$, this string operator becomes the identity, $\hat{S}_{pq} = 1$ and \hat{H} becomes quadratic in the Majorana operators. Consequently, the model can be described by free fermions and is therefore exactly solved by a FGS [22]. In general, however, for the long-range TFIM we will need to include the contribution of the operator \hat{S}_{pq} . To avoid ambiguity, we use the term *long-range* in this paper for all systems with $\alpha < \infty$, since the spin interaction breaks up into a sum of terms proportional to $1/|p-q|^\alpha$, where all lattice sites p, q give nonzero contributions, and not just nearest-neighbour sites $p, p+1$ (as in the special case $\alpha \rightarrow \infty$). Often times, the term *long-range* is reserved in literature for nonadditive systems with an algebraic exponent $\alpha = \sigma + d$ in a d -dimensional system for $\sigma < 0$ (which in a one-dimensional system refers to the regime $\alpha < 1$) [26–28]. Thus, to avoid confusion, in our paper we will refer to $\alpha < 1$ as the *strong* long-range, and to $\alpha > 1$ as the *weak* long-range regime, while the special case $\alpha = 1$ marks the boundary of both regimes.

B. Fermionic Gaussian states

The formal definition of a FGS is given by [22]

$$\hat{\rho}_{\text{GS}} = \text{tr} \left(e^{-\beta \hat{H}_{\text{GS}}} \right)^{-1} e^{-\beta \hat{H}_{\text{GS}}}, \quad (3)$$

where $\hat{H}_{\text{GS}} = \frac{i}{4} \hat{\mathbf{a}}^T \mathbf{G} \hat{\mathbf{a}}$ is a Hermitian operator, $\beta \in \mathbb{R}$, $\hat{\mathbf{a}} = (\hat{a}_1, \hat{a}_2, \dots, \hat{a}_{2N})^T$ is a column vector of Majorana operators, and \mathbf{G} is a $(2N \times 2N)$ real-valued and antisymmetric matrix. FGS are fully described by the real and antisymmetric covariance matrix $\mathbf{\Gamma}$ with entries

$$\Gamma_{lm} = \frac{i}{2} \text{tr}(\hat{\rho}_{\text{GS}}[\hat{a}_l, \hat{a}_m]), \quad (4)$$

$l, m \in \{1, 2, \dots, 2N\}$, and where $[\hat{A}, \hat{B}] = \hat{A}\hat{B} - \hat{B}\hat{A}$ denotes the commutator of two operators \hat{A}, \hat{B} . While Eqs. (3) and (4) describe both pure and mixed FGS, we only focus on pure FGS in this paper, since we are interested in the ground state. Pure FGS are characterized by $\mathbf{\Gamma}^2 = -\mathbf{1}_{2N}$ [$\mathbf{1}_k$ denotes the $(k \times k)$ -identity matrix], and eigenvalues of the covariance matrix are given by $\lambda \in \{-1, 1\}$. All information contained

in the density matrix (3) of a FGS is also contained in its covariance matrix (4). The expectation value of a product of Majorana or fermionic operators can be computed efficiently through Wick's theorem [22,29],

$$\text{tr}(\hat{\rho}_{\text{GS}}\hat{a}_{i_1}\hat{a}_{i_2}\cdots\hat{a}_{i_{2m}}) = (-i)^m \text{Pf}(\mathbf{\Gamma}|_{i_1 i_2 \dots i_{2m}}), \quad (5)$$

where $i_1 \neq i_2 \neq \dots \neq i_{2m}$ for $i_k \in \{1, \dots, 2N\}$ and $k = 1, \dots, 2N$. The matrix $\mathbf{\Gamma}|_{i_1 i_2 \dots i_{2m}}$ denotes a $(2m \times 2m)$ -submatrix of $\mathbf{\Gamma}$ with the corresponding rows and columns i_1, i_2, \dots, i_{2m} , and $\text{Pf}(\mathbf{A})$ denotes the Pfaffian of a skew-symmetric matrix \mathbf{A} .

C. Approximating the ground state with a fermionic Gaussian state

Using Wick's theorem (5), we are able to compute the energy expectation value

$$E(\mathbf{\Gamma}) = \text{tr}(\hat{\rho}_{\text{GS}}\hat{H}), \quad (6)$$

which results in

$$E(\mathbf{\Gamma}) = - \sum_{p=1}^N \frac{\hbar_p}{2} (\Gamma_{2p-1, 2p} - \Gamma_{2p, 2p-1}) + \sum_{p < q}^N J_{pq} (-1)^{q-p} \text{Pf}\{\mathbf{\Gamma}|_{2p, 2p+1, \dots, 2q-1}\}, \quad (7)$$

for the Hamiltonian given by Eq. (1). In order to approximate the ground state of the Hamiltonian within the family of FGS, one has to find a covariance matrix $\mathbf{\Gamma}$, which minimizes $E(\mathbf{\Gamma})$. While one can apply any constrained optimization method, in the following, we will discuss two particular algorithms for finding the optimal $\mathbf{\Gamma}$, which we will use in Sec. III.

(a.) *Imaginary time evolution (ITE)*. The first algorithm performs an imaginary time evolution (ITE) under the constraint that Wick's theorem holds throughout the evolution. This constraint guarantees that the evolved state remains a FGS, and leads to an equation of motion for the corresponding covariance matrix,

$$\frac{d\mathbf{\Gamma}}{d\tau} = \frac{1}{2} [\mathbf{\Gamma}, [\mathbf{\Gamma}, \mathbf{H}^{(\text{mf})}]], \quad (8)$$

where $\tau \in \mathbb{R}$ denotes the imaginary time. We derive Eq. (8) in Appendix A. The central quantity herein is the mean-field Hamiltonian $\mathbf{H}^{(\text{mf})}(\mathbf{\Gamma})$, which is the gradient of the energy with respect to the covariance matrix,

$$H_{lm}^{(\text{mf})} = 4 \frac{dE(\mathbf{\Gamma})}{d\Gamma_{lm}}. \quad (9)$$

Note, that the mean-field Hamiltonian $\mathbf{H}^{(\text{mf})}$ is by construction an antisymmetric matrix. This term can be computed explicitly by using identities for the matrix derivative of a Pfaffian, which we have derived in Appendix B.

We solve Eq. (8) iteratively, by discretizing the ITE into small time steps $\Delta\tau$. Starting from a random initial covariance matrix, we evolve the covariance matrix through $\mathbf{\Gamma}(\tau + \Delta\tau) \approx \mathbf{O}(\Delta\tau)\mathbf{\Gamma}(\tau)\mathbf{O}(\Delta\tau)^T$, where $\mathbf{O}(\Delta\tau) = e^{\frac{1}{2}[\mathbf{H}^{(\text{mf})}, \mathbf{\Gamma}]\Delta\tau}$ is an orthogonal matrix. As explicitly shown in Ref. [23], this approach preserves the purity of the FGS, while ensuring a monotonic decrease of the energy in each iteration.

(b.) *Zero temperature (ZT)*. The second algorithm uses a self-consistent equation for the steady-state solution of Eq. (8). In this algorithm, for a given $\mathbf{\Gamma}$, we diagonalize the mean-field matrix $i\mathbf{H}^{(\text{mf})} = \mathbf{U}\mathbf{D}\mathbf{U}^\dagger$ and recalculate

$$\mathbf{\Gamma} = i\mathbf{U}\text{sgn}(\mathbf{D})\mathbf{U}^\dagger. \quad (10)$$

Here, \mathbf{U} is a unitary matrix, \mathbf{D} is a diagonal matrix containing the real eigenvalues of $i\mathbf{H}^{(\text{mf})}$, and $\text{sgn}(\mathbf{D})$ is the sign function applied to the diagonal entries of \mathbf{D} . From this $\mathbf{\Gamma}$ we recalculate $i\mathbf{H}^{(\text{mf})}$ and repeat the procedure until the covariance matrix is converged. One can check that the solution of this algorithm is also a stationary state of Eq. (8) with $\mathbf{\Gamma}^2 = -\mathbf{1}$.

In both algorithms we choose several random initial covariance matrices $\mathbf{\Gamma}_{\text{init}}$ to ensure unbiased results. A random $\mathbf{\Gamma}_{\text{init}}$ is generated through $\mathbf{\Gamma}_{\text{init}} = \mathbf{O}^T \mathbf{\Omega} \mathbf{O}$, where \mathbf{O} is a random orthogonal matrix and we defined the block diagonal matrix $\mathbf{\Omega} = \bigoplus_{k=1}^N (-1)^{r_k} \begin{pmatrix} 0 & 1 \\ -1 & 0 \end{pmatrix}$, where $r_k \in \{0, 1\}$ is chosen randomly and \bigoplus denotes the direct sum. After convergence of the corresponding algorithm we achieve a stationary solution $\mathbf{\Gamma}_{\text{st}}$. With the help of this solution we can then find the GHF approximation to the ground-state energy given by $E(\mathbf{\Gamma}_{\text{st}})$. Besides the energy and entanglement entropy introduced in the following section, the covariance matrix allows us direct access to quantum correlations.

(c.) *Algorithmic cost*. The computational cost of performing GHF scales as $\mathcal{O}(N^3)$, as it involves diagonalizations of a quadratic fermionic Hamiltonian [30,31]. The cost of DMRG, which we used and referenced in our paper scales as $\mathcal{O}(N\chi^3)$, where χ is the employed bond dimension of the underlying matrix product state and N is the system size [32]. The maximum bipartite entanglement that an MPS can reach is bounded by $\log(\chi)$. Therefore, χ needs to grow exponentially with the entanglement for DMRG to give an accurate description of a corresponding quantum state [31,32]. For the one-dimensional case studied here, the entanglement entropy can scale up to logarithmically with the system size, leading to a computational cost of DMRG of $\mathcal{O}(N^4)$, indicating the computational scaling advantage of GHF over DMRG. Note, that this computational scaling advantage becomes more pronounced if one were to consider higher-dimensional systems.

D. Entanglement entropy and central charge

Entanglement entropy is a well-studied measure for the amount of quantum correlations in a pure quantum state [33,34]. Let \mathcal{A}, \mathcal{B} be a bipartition of the full quantum system. The entanglement entropy is defined as $S_{N_{\mathcal{A}}} = -\text{tr}(\hat{\rho}_{\mathcal{A}} \log(\hat{\rho}_{\mathcal{A}}))$, where \mathcal{A} describes a subsystem containing $N_{\mathcal{A}}$ spins. The reduced density matrix $\hat{\rho}_{\mathcal{A}} = \text{tr}_{\mathcal{B}}(\hat{\rho})$ is obtained by performing a partial trace over the disjoint subsystem \mathcal{B} , with $N_{\mathcal{B}} = N - N_{\mathcal{A}}$ spins. For the spins numbered as $\mathcal{A} = \{1, 2, \dots, N/2\}$ we label the corresponding Majorana operator indices by $\mathfrak{M}_{\mathcal{A}} = \{1, 2, \dots, N-1, N\}$. The entanglement entropy is then fully determined by the matrix $\mathbf{\Gamma}_{\mathcal{A}} = \mathbf{\Gamma}|_{\mathfrak{M}_{\mathcal{A}}}$ and can be calculated with [23,35,36]

$$S_{N/2} = \frac{N}{2} \log(2) - \frac{1}{2} \text{tr}[(\mathbf{1}_N + i\mathbf{\Gamma}_{\mathcal{A}}) \log(\mathbf{1}_N + i\mathbf{\Gamma}_{\mathcal{A}})]. \quad (11)$$

For short-range 1D systems, the entanglement entropy typically follows two different scalings: for gapped phases, $S_{N/2}$ saturates to a constant value independent of N and thus obeys the so-called area law [37]. For gapless phases, the entanglement entropy exhibits the following behavior [38]:

$$S_{N/2} = \frac{c}{6} \log(N) + B, \quad (12)$$

where c is the central charge characterizing the universality class of the system and B is a nonuniversal constant. For the nearest-neighbour TFIM at $\alpha = \infty$ the value of $c = 1/2$ can be found exactly.

For long-range systems we need to distinguish between *weak* long-range interactions, $\alpha > d = 1$, and the *strong* long-range interactions, $\alpha < d = 1$.

For *weak* long-range interactions and a nonvanishing energy gap we expect also an area-law scaling, implying that $S_{N/2}$ is independent of N . For the case of a vanishing gap one also finds a logarithmic divergence [37,39–41] following Eq. (12).

For *strong* long-range interactions in the AFM-TFIM we expect instead a logarithmic divergence of the entanglement entropy, where $S_{N/2}$ obeys Eq. (12) and one can find $c \neq 0$ even in presence of a nonvanishing gap [42–45]. In this regime c is strictly speaking not a central charge but because of the same functional dependence of $S_{N/2}$ in Eq. (12), we also denote c as the effective central charge.

III. RESULTS

A. Phase diagram

In this section, we show that a computationally inexpensive GHF mean-field approach can reproduce the phase diagram of the AFM-TFIM for a wide range of values α , both in the weak and strong long-range regime, and is able to locate the point of the phase transition for $\alpha \geq 1$ in excellent agreement with state-of-the-art numerical methods.

As a first benchmark and in the same spirit of Ref. [6] we map the phase diagram by calculating the entanglement entropy for a wide range of values of α , from *weak* to *strong* long-range interactions, and for $\theta \in (0, \pi/2)$. The values of $S_{N/2}$ [Eq. (11)] computed with the ZT GHF method are visible in Fig. 1 for $N = 100$. For $\theta = 0$ the interactions vanish and $S_{N/2} = 0$ for all values of α . This represents the phase where all spins are uncorrelated and align with the external magnetic field. However, when θ and therefore the AFM interactions are increased, the minimization of the interaction energy competes with the external magnetic field. This is accompanied by an increase of $S_{N/2}$. Dependent on α , there is a critical value $\theta_c(\alpha)$ beyond which the spins favor an AFM order. This transition is highlighted in Fig. 1 by a sharp rise of $S_{N/2}$. Our findings are in qualitative agreement with the ones obtained in Ref. [6] from DMRG calculations. To compare our results also quantitatively, we will now focus on the *weak* and *strong* long-range interactions cases separately.

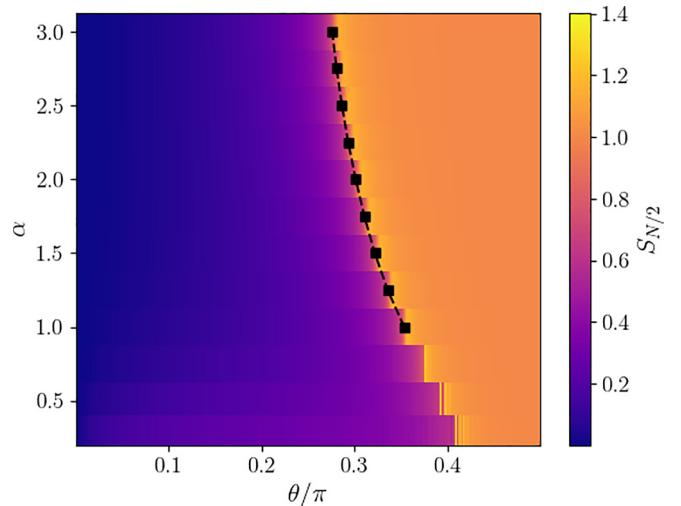


FIG. 1. We plot the entanglement entropy $S_{N/2}$ from the covariance matrix obtained through the ZT algorithm for a system size $N = 100$, $\alpha \in \{0.30, 0.50, 0.75, 1.00, \dots, 3.00\}$, and $\theta \in (0, \pi/2)$. For the color coding we use the color map “plasma” in the python package “matplotlib”. Black squares represent the quantum critical points θ_c^∞/π in the thermodynamic limit, which are listed in Table I, while the dashed line serves as a guide to the eye.

B. Weak long-range interactions

1. Comparison of GHF and DMRG

For *weak* long-range interactions, $\alpha \geq 1$, we show the ground-state energy and the entanglement entropy in Fig. 2(a) and Fig. 2(b), respectively.

The solid lines represent the results obtained from the GHF theory while hollow markers represent the results obtained from DMRG simulations. Both simulation methods predict a rather smooth behavior of the energy in Fig. 2(a). For larger values of $\alpha \geq 1.5$ we find a maximum and a decrease beyond the maximum point. The GHF and DMRG simulations agree perfectly.

The entanglement entropy, visible in Fig. 2(b), shows for all values and both simulation methods a very quick increase

TABLE I. The critical points θ_c^∞/π obtained from Eq. (13) with FGS and ZT, in comparison to LCE [10], and DMRG [6], DMRG* [8] results. The values are obtained for various exponents α and for simulations up to $N = 100$ spins. The error indicated in the FGS column in round brackets is the standard deviation for the intersect of a linear regression fit of θ_{\max}/π as a function of $1/N$.

$\alpha \backslash \theta_c^\infty/\pi$	FGS	LCE	DMRG	DMRG*
1.00	0.3534(4)		0.3509	
1.25	0.3357(1)	0.35(5)		
1.50	0.3218(1)	0.3213(5)	0.3226	
1.75	0.3106(1)			
2.00	0.3013(2)	0.3026(8)	0.3027	0.3021
2.25	0.2932(2)	0.294(4)		
2.50	0.2865(1)	0.2871(11)		
2.75	0.2807(2)			
3.00	0.2760(2)	0.27722(25)	0.2782	

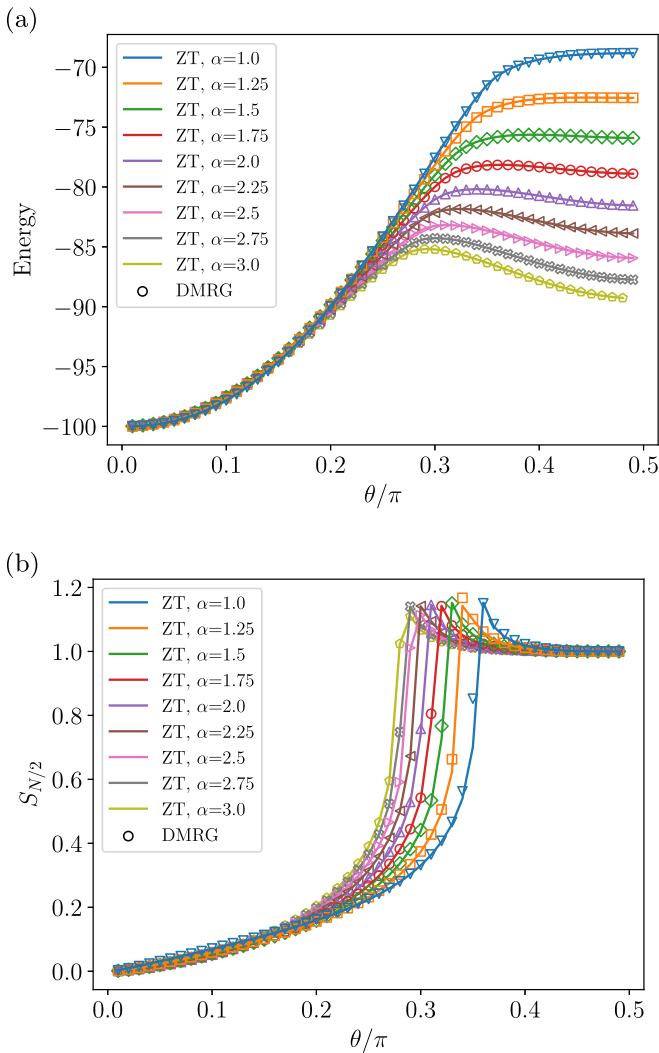


FIG. 2. For a system of size $N = 100$ and exponents $\alpha \in [1, 3]$, we plot (a) the energy E and (b) the entanglement entropy $S_{N/2}$ (bottom), as defined in Eqs. (6) and (11), obtained from the covariance matrix of the ZT algorithm (solid lines) and compare it to DMRG (hollow markers).

and a pronounced singularity. The latter is an indicator for the phase transition point. Beyond this point we find again a decrease of the entanglement entropy. Both methods, GHF and DMRG, are in very good agreement, see Appendix C for more details.

2. Threshold and central charge

In order to find a value for the threshold at $N \rightarrow \infty$, we are performing a finite-size scaling. For this we carry out analog simulations for a range of smaller system sizes $N \in \{20, 30, \dots, 100\}$. Then we find numerically the maximum of the entanglement entropy of the half chain $S_{\max} = S_{N/2}(\theta_{\max})$ and the corresponding value θ_{\max} . The latter is found using the optimizer `scipy.optimize.fminbound()`, which is pre-implemented in python. For every value θ examined by the optimizer we find the optimal FGS for the corresponding Hamiltonian. Optimizing $S_{N/2}$ over θ can be achieved as FGS provide a way for calculating $S_{N/2}$ polynomially in N ,

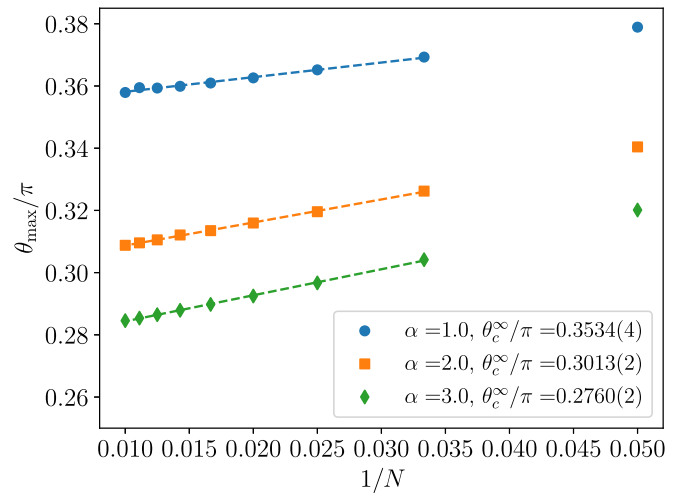


FIG. 3. Example for the fit of Eq. (13) to the value of θ_{\max} obtained by maximization of the entanglement entropy S with FGS. The thresholds θ_c^∞/π are shown for the respective cases $\alpha \in \{1, 2, 3\}$, see Table I for more details.

see Eq. (11). We then use the following finite-size scaling law [46]:

$$\theta_{\max}(N) = \theta_c^\infty + \frac{a}{N}, \quad (13)$$

where θ_c^∞ is the threshold at $N \rightarrow \infty$ and a is a fitting parameter, which determines the finite-size scaling. Fitting Eq. (13) to the numerically obtained data of θ_{\max} reveals the θ_c^∞ in the thermodynamic limit [47]. In Fig. 3 we provide examples for the fits that are used to calculate θ_c^∞ . We perform these fits for various values of α and the results for the threshold are collected in Table I. In addition, we have plotted the results of θ_c^{\max} in Fig. 1 as black squares, which mark the sudden spike of the entanglement entropy. In Table I we compare the results obtained from the GHF theory with the ones obtained from LCE calculations [10], DMRG data of Ref. [6] (labeled DMRG) and Ref. [8] (labeled DMRG*). We find in general very good agreement of the thresholds obtained from the different methods.

Besides the threshold θ_c^∞ we can also extract the scaling of the maximum entropy $S_{\max} = S(\theta_{\max})$. At the critical point we use the scaling law [38] given by Eq. (12). We fit Eq. (12) to the maximum values S_{\max} as displayed in Fig. 4(a). From these fits we extract the central charge c , which is shown in Fig. 4(b) as function of α . The central charge is always above the result $c = 1/2$ expected from the short-range TFIM. We also compare our results to different DMRG results of Ref. [6,8]. We find that the central charges obtained from FGS are systematically smaller than the values provided by Ref. [6] and larger than the DMRG results of Ref. [8]. The central charge c is monotonically decreasing in the weak long-range regime, but drops at the onset of the strong long-range regime at $\alpha = 1$. In conclusion, we found that the results of the GHF method are in good qualitative and quantitative agreement with state-of-the-art numerical methods for *weak* long-range interactions.

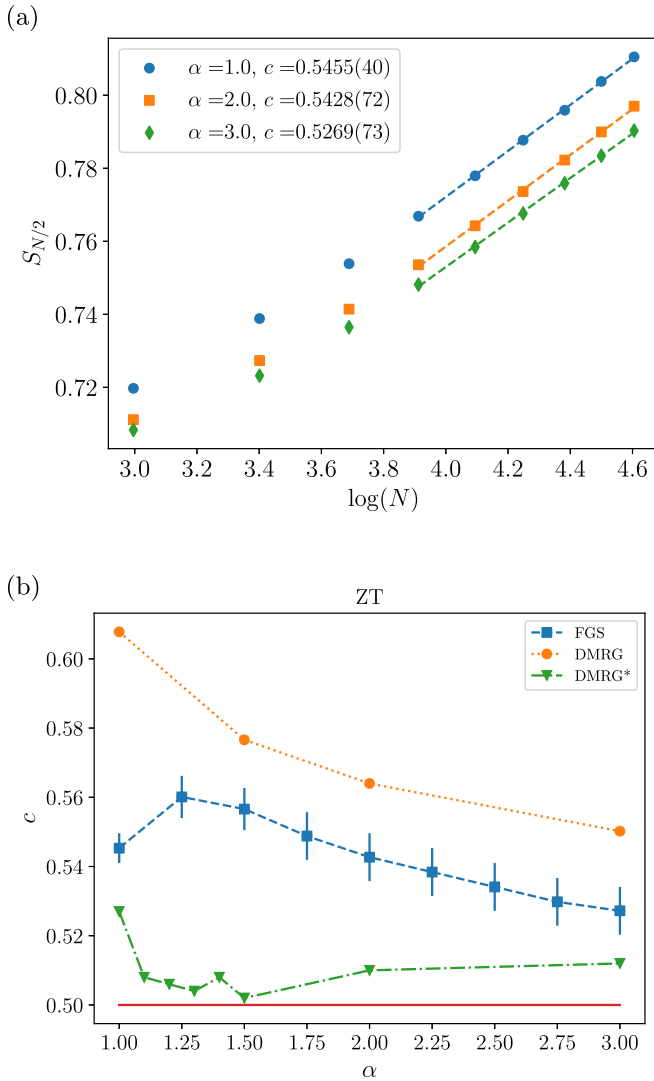


FIG. 4. (a) Extracting the central charge. Using the ZT algorithm for various α , here exemplified by $\alpha \in \{1, 2, 3\}$, we plot the entanglement entropy $S_{N/2}$ against $\log(N)$. For each α we perform a linear regression fit, neglecting the system sizes $N \in \{20, 30, 40\}$ to mitigate finite-size effects. (b) Central charge c obtained from finite-size scaling up to system size $N = 100$ of FGS evolutions through the ZT algorithm (blue squares) for the AFM long-range TFIM. For comparison, DMRG results from finite-size scaling of system sizes of up to $N = 100$ from Ref. [6] (“DMRG”, orange square) and [8] (“DMRG*”, green triangles) are included. The red horizontal line represents the value $c = 1/2$, which describes the Ising universality class. Error bars represent the standard deviation from the linear regression fit.

C. Strong long-range interactions

1. Comparison of GHF and DMRG

We will now shift our focus to the regime of *strong* long-range interactions, $\alpha < 1$. We first plot the ground-state energy and the entanglement entropy in Fig. 5(a) and Fig. 5(b) for three different values of $\alpha < 1$ of size $N = 100$. In Fig. 5(a) we obtain for all three values of α a monotonously increasing energy with θ . This is different to the case of *weak* long-range interactions [see Fig. 2(a)] where we have

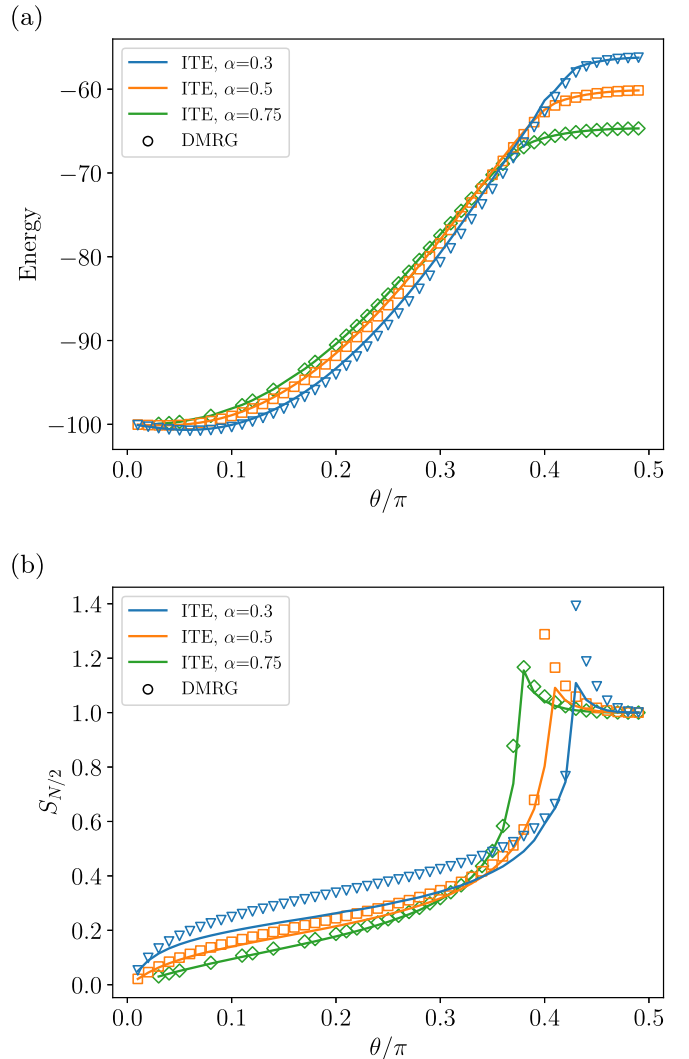


FIG. 5. (a) Energy and (b) entanglement entropy obtained from the covariance matrix of the ITE algorithm (solid lines) and DMRG (empty markers) simulations for $N = 100$ and $\alpha \in \{0.3, 0.5, 0.75\}$.

observed a maximum close to the threshold at least for sufficiently large $\alpha \geq 1.5$. We compare our results obtained from FGS also with the ones obtained from DMRG results. Here, we find that DMRG always predicts a lower ground-state energy. The discrepancy of the two methods is even more striking in the entanglement entropy visible in Fig. 5(b). Here, while we still observe very good agreement for $\alpha = 0.75$ we found clear deviations for $\alpha = 0.3$ and $\alpha = 0.5$. The DMRG results predict tendentially a larger entanglement entropy than the FGS. This is an indicator that FGS are less well suited for the description of the TFIM for very small α , i.e., very strong long-range interactions.

2. Violations to the area law

We will now analyze the scaling of the entanglement entropy with the system size. For this we calculate the entanglement entropy for various parameters θ and α and for different numbers of spins $N \in \{40, 50, \dots, 100\}$. We then fit the coefficients c and B using Eq. (12) to the obtained values

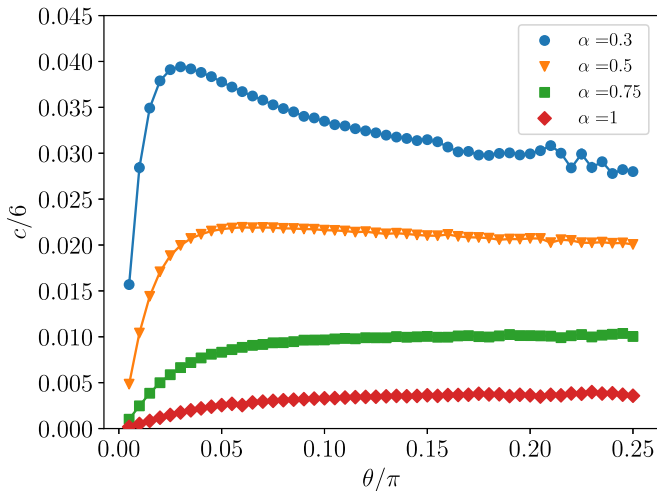


FIG. 6. Violations to the area law. The effective central charge c [Eq. (12)] calculated from finite scaling of system sizes $N \in \{40, 50, \dots, 100\}$ for 50 different values deep in the gapped region $\theta \in (0, \pi/4)$ for the GHF ITE algorithm. Error bars for the standard deviation are also included, but too small to be visible. Solid lines connecting the markers serve as a guide to the eye.

of the entanglement entropy. The obtained values of c are shown in Fig. 6. At this point we remark that the effective central charge c is calculated far away from the threshold in a phase with a nonvanishing energy gap [6]. As mentioned at the end of Sec. IID, the behavior of the strong-long-range regime for values θ far away from θ_c^∞ differs here significantly from the weak-long-range regime. While one expects an effective central charge $c = 0$ in the latter, the strong-long-range regime displays an effective central charge $c \neq 0$ that follows Eq. (12).

For the values $\alpha < 1$, we find $c = 0$ only at $\theta = 0$. For increasing θ we find a sharp increase of c . For $\alpha = 0.3$ and $\alpha = 0.5$ we find a maximum and then a decrease again for larger values of θ . A qualitatively similar behavior has also been observed in Ref. [6]. This is a violation to the area law where the logarithmic divergence does not originate from a closing gap in the spectrum of the system [6]. Our GHF results exhibit the most significant deviations from DMRG close to the maximum values θ_{\max} at $\alpha = 0.3$ and $\alpha = 0.5$. This also suggests a potential discrepancy of the obtained thresholds that can be obtained from the two methods. This also suggest a potential discrepancy of the obtained thresholds that can be obtained from the two methods. We therefore conclude that the FGS are able to predict this feature, although the quantitative values deviate from the ones obtained from DMRG results.

IV. SUMMARY AND OUTLOOK

This paper presents an extensive study of the AFM long-range TFIM in both the weak and strong long-range regime using generalized Hartree Fock theory, a mean-field method with low computational cost. We validate our results by comparing the computed energy and entanglement entropy to DMRG. We plot the phase diagram and provide estimates for

the location of the critical point of the second-order phase transition through finite-size scaling for $\alpha \in [1, 3]$ and find that they are in excellent agreement with both LCE calculations of Ref. [10] and DMRG simulations of Refs. [6,8]. At the critical point, we compute the central charge c of the underlying conformal field theory for $\alpha \in \{0.3, 0.5, 1\}$, and find $c > 1/2$ for all values of α . In the strong long-range regime we still found qualitative agreement between FGS and DMRG calculations. Hereby we found larger quantitative deviations for smaller values of α . Remarkably, GHF can predict the logarithmic violations to the area law in the AFM-TFIM, which has previously been studied with DMRG. Based on these findings, we conclude that FGS provide a numerically inexpensive alternative to study the AFM long-range TFIM and that our results are in good agreement with DMRG, the current state-of-the-art numerical method for one-dimensional lattice systems.

All GHF simulations were carried out using a standard laptop computer. Since the dimensionality of the system only appears in the Hamiltonian elements h_{pq} and J_{pq} , it is straightforward to apply FGS to the two- and three-dimensional TFIM. Therefore, it would be interesting to compare FGS simulations with methods that can be applied to the two-dimensional AFM-TFIM [10]. Moreover, while we have focused on the AFM regime, FGS can readily be applied to the ferromagnetic regime $\theta \in (-\pi, 0)$. In this paper we have focused on the entanglement entropy; however, we remark that GHF gives also access to quantities such as correlation functions and the entanglement spectrum that can be extracted directly from the covariance matrix and using Wick's theorem. FGS can also be used to study dynamics under the evolution of the TFIM, with equations of motion similar to Eq. (8) [23,24]. In particular, this would enable an efficient simulation of entanglement dynamics after a parameter quench for spins with short- to long-range interactions [48]. From a numerical standpoint, more efficient calculations of the central quantities such as Eq. (7) could lead to dramatic computational speedups. As a possible pathway, it would be interesting to see if sum identities for Pfaffians such as provided in Refs. [49–51] could be applied to the TFIM Hamiltonian in order to achieve more efficient calculations of the energy and mean-field Hamiltonians. Finally, one could study if different spin-to-fermion mappings [52–54], each resulting in a different form of H when expressed in fermionic operators, have an effect on the FGS simulations and the obtained values of ground-state energy and entanglement entropy.

ACKNOWLEDGMENTS

The authors thank Kai Phillip Schmidt for providing the data for the LCE calculations from Ref. [10] and Luca Tagliacozzo for providing the DMRG data from Ref. [6]. The authors also thank Giovanna Morigi for insightful discussions. M.P.K. thanks Miguel Ángel Martín-Delgado and Frank Wilhelm-Mauch for helpful discussions and support. S.B.J. acknowledges support from the Research Centers of the Deutsche Forschungsgemeinschaft (DFG): Projects A4 and A5 in SFB/Transregio 185: "OSCAR."

APPENDIX A: DERIVATION OF THE EQUATIONS OF MOTION FOR THE ITE ALGORITHM

In this Appendix, we will derive Eq. (8), which describes the imaginary-time evolution of a FGS. Equation (8) was also shown in Ref. [23] for fourth-order polynomials of fermionic operators and for an even more general case in Ref. [24].

We start by writing down the imaginary-time evolution for the pure FGS $\hat{\rho}_{\text{GS}} = |\Psi_{\text{GS}}\rangle\langle\Psi_{\text{GS}}|$ determined by

$$\frac{d}{d\tau}|\Psi_{\text{GS}}\rangle = -(\hat{H} - \langle\Psi_{\text{GS}}|\hat{H}|\Psi_{\text{GS}}\rangle)|\Psi_{\text{GS}}\rangle. \quad (\text{A1})$$

The pure FGS can be generated by a Gaussian transformation

$$|\Psi_{\text{GS}}\rangle = \hat{U}_{\text{GS}}|\text{vac}\rangle, \quad (\text{A2})$$

where $|\text{vac}\rangle$ denotes the fermionic vacuum and

$$\hat{U}_{\text{GS}}(\xi) = e^{i\hat{\mathbf{a}}^T \xi \hat{\mathbf{a}}} \quad (\text{A3})$$

describes the generator of a pure FGS [22]. Here, ξ denotes a $(2n \times 2n)$ antisymmetric and Hermitian matrix (the matrix elements $\xi_{kl} = -\xi_{lk}$ are purely imaginary). To calculate the covariance matrix Γ we use

$$\Gamma = -\mathbf{U}_\xi \Upsilon \mathbf{U}_\xi^T, \quad (\text{A4})$$

where

$$\Upsilon = \bigoplus_{p=1}^N \begin{pmatrix} 0 & 1 \\ -1 & 0 \end{pmatrix}. \quad (\text{A5})$$

is the covariance of the vacuum state and where we employed the transformation

$$\hat{U}_{\text{GS}}^\dagger(\xi) \hat{\mathbf{a}} \hat{U}_{\text{GS}}(\xi) = \mathbf{U}_\xi \hat{\mathbf{a}}, \quad (\text{A6})$$

with

$$\mathbf{U}_\xi = e^{i\xi}. \quad (\text{A7})$$

Now, the idea is that we derive from Eq. (A1) a differential equation for \mathbf{U}_ξ , which can then be used to calculate Γ using Eq. (A4). For this we treat the left- and right-hand side of Eq. (A1) separately and rewrite it as

$$\hat{U}_{\text{GS}} \hat{L} |\text{vac}\rangle = \hat{U}_{\text{GS}} \hat{R} |\text{vac}\rangle. \quad (\text{A8})$$

We then expand the operators \hat{L} and \hat{R} up to second order in terms of normal-ordered monomials of the Majorana operators and apply them to the vacuum state.

(a.) *Left-hand side of Eq. (A1).* The operator \hat{L} is defined as

$$\hat{L} = \hat{U}_{\text{GS}}^\dagger \left(\frac{d\hat{U}_{\text{GS}}(\xi)}{d\tau} \right). \quad (\text{A9})$$

The derivative of the unitary transformation is given by

$$\frac{d\hat{U}_{\text{GS}}(\xi)}{d\tau} = \hat{U}_{\text{GS}}(\xi) \left[\frac{i}{4} \hat{\mathbf{a}}^T \mathbf{U}_\xi^T \frac{d\mathbf{U}_\xi}{d\tau} \hat{\mathbf{a}} \right]. \quad (\text{A10})$$

Here, we have used Eq. (A3), the identity [55]

$$\frac{de^{\hat{J}(\tau)}}{d\tau} = \int_0^1 du e^{(1-u)\hat{J}(\tau)} (d_\tau \hat{J}(\tau)) e^{u\hat{J}(\tau)}, \quad (\text{A11})$$

and the orthogonality property $\mathbf{U}_\xi \mathbf{U}_\xi^T = \mathbf{1}$. For the normal-ordered expression we therefore find

$$\hat{L} = \hat{L}_0 + \hat{L}_2, \quad (\text{A12})$$

with

$$\hat{L}_0 = \frac{i}{4} \text{tr} \left[\frac{d\mathbf{U}_\xi}{d\tau} \mathbf{U}_\xi^T \Gamma \right], \quad (\text{A13})$$

$$\hat{L}_2 = \frac{1}{4} : \hat{\mathbf{a}}^T \mathbf{U}_\xi^T \frac{d\mathbf{U}_\xi}{d\tau} \hat{\mathbf{a}} :, \quad (\text{A14})$$

where $: \hat{A} :$ denotes the elementwise normal ordering of \hat{A} .

(b.) *Right-hand side of Eq. (A4).* The definition of \hat{R} is

$$\hat{R} = -\hat{U}_{\text{GS}}^\dagger (\hat{H} - \langle\Psi_{\text{GS}}|\hat{H}|\Psi_{\text{GS}}\rangle) \hat{U}_{\text{GS}}. \quad (\text{A15})$$

We can now use a modification of Wick's theorem to calculate

$$\hat{U}_{\text{GS}}^\dagger \hat{H} \hat{U}_{\text{GS}} = \langle\Psi_{\text{GS}}|\hat{H}|\Psi_{\text{GS}}\rangle + \frac{i}{4} : \hat{\mathbf{a}}^T \mathbf{U}_\xi^T \mathbf{H}^{(\text{mf})} \mathbf{U}_\xi \hat{\mathbf{a}} : + \tilde{Q}, \quad (\text{A16})$$

where \tilde{Q} collects all normally ordered monomials of quartic order or higher. We derive this expression in Appendix B. Inserting Eq. (A16) into Eq. (A15), we find for \hat{R} the following expression:

$$\hat{R} = \hat{R}_2 - \tilde{Q}, \quad (\text{A17})$$

with

$$\hat{R}_2 = -\frac{i}{4} : \hat{\mathbf{a}}^T \mathbf{U}_\xi^T \mathbf{H}^{(\text{mf})} \mathbf{U}_\xi \hat{\mathbf{a}} :. \quad (\text{A18})$$

(c.) *Comparing left- and right-hand side.* We now require to match $\hat{L}|\text{vac}\rangle$ and $\hat{R}|\text{vac}\rangle$ up to second order. This is a consequence of our restriction to FGS. Therefore, we find two equations

$$\hat{L}_0 |\text{vac}\rangle = 0, \quad (\text{A19})$$

$$\hat{L}_2 |\text{vac}\rangle = \hat{R}_2 |\text{vac}\rangle, \quad (\text{A20})$$

from which we wish to derive the equations of motion of the ITE. We first consider Eq. (A20),

$$: \hat{\mathbf{a}}^T \mathbf{U}_\xi^T \frac{d\mathbf{U}_\xi}{d\tau} \hat{\mathbf{a}} : |\text{vac}\rangle = -i : \hat{\mathbf{a}}^T \mathbf{U}_\xi^T \mathbf{H}^{(\text{mf})} \mathbf{U}_\xi \hat{\mathbf{a}} : |\text{vac}\rangle. \quad (\text{A21})$$

For any normal-ordered polynomial of fermionic operators applied to the vacuum state, the only terms that do not vanish are polynomials, which exclusively contain fermionic creation operators. Therefore, we define the vector

$$\mathbf{r} = \hat{\mathbf{c}}^\dagger \otimes \begin{pmatrix} 1 \\ i \end{pmatrix}, \quad (\text{A22})$$

where $\hat{\mathbf{c}}^\dagger = (\hat{c}_1^\dagger, \dots, \hat{c}_N^\dagger)$, and rewrite Eq. (A21) in terms of fermionic creation and annihilation operators, which leads to

$$\hat{\mathbf{r}}^T \mathbf{U}_\xi^T \frac{d\mathbf{U}_\xi}{d\tau} \hat{\mathbf{r}} |\text{vac}\rangle = -i \hat{\mathbf{r}}^T \mathbf{U}_\xi^T \mathbf{H}^{(\text{mf})} \mathbf{U}_\xi \hat{\mathbf{r}} |\text{vac}\rangle, \quad (\text{A23})$$

where the normal ordering “ $:$ ” may now be dropped. We would now like to compare the matrices of Eq. (A23). However, before doing so, we need to take into account the symmetry operations, which leave the operator $\hat{\mathbf{r}}$ invariant. For this, we first rewrite Υ defined in Eq. (A5) as $\Upsilon = \mathbf{1}_N \otimes$

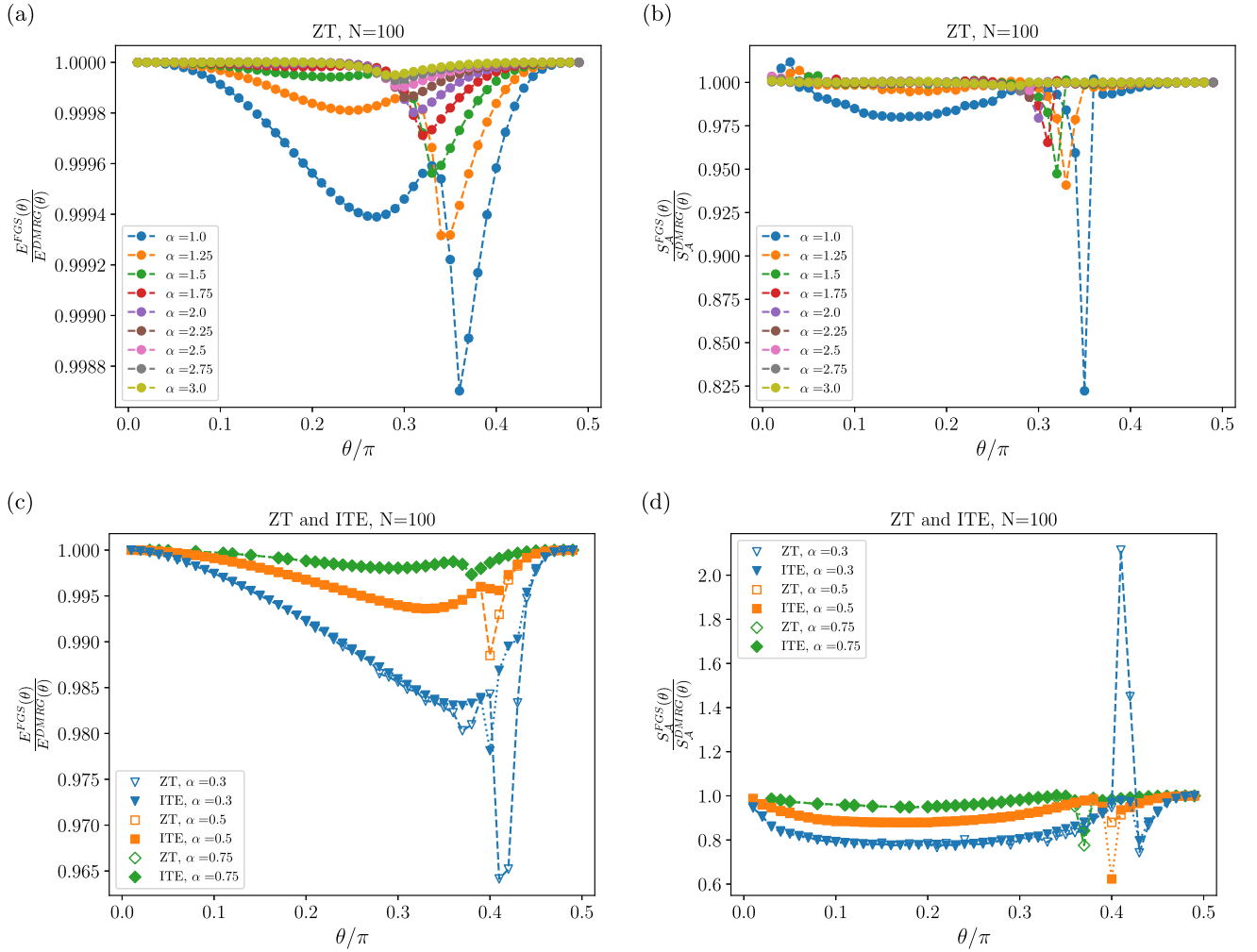


FIG. 7. Energy expectation E^{FGS} (a) and entanglement entropy S^{FGS} (b) obtained from GHF ZT simulations in relation to E^{DMRG} and S^{DMRG} calculated from DMRG simulation as function of θ . The results are obtained for the AFM-TFIM of size $N = 100$ and various values of α in the weak-long-range regime. [(c),(d)] Same as (a) and (b), but for values of α in the strong-long-range regime, including GHF simulation results for both, the GHF ITE and ZT algorithms.

$\begin{pmatrix} 0 & 1 \\ -1 & 0 \end{pmatrix}$). Thus, the symmetry operations on the operators are given by $-i\Upsilon\hat{\mathbf{r}} = \hat{\mathbf{r}}$ and $i\hat{\mathbf{r}}^T\Upsilon = \hat{\mathbf{r}}^T$. The real-valued skew-symmetric solution for $\frac{d\mathbf{U}_\xi}{d\tau}$, which satisfies Eq. (A19) is then given by

$$\frac{d\mathbf{U}_\xi}{d\tau} = -\frac{1}{2}\mathbf{\Gamma}\mathbf{H}^{(mf)}\mathbf{U}_\xi - \frac{1}{2}\mathbf{H}^{(mf)}\mathbf{U}_\xi\Upsilon. \quad (\text{A24})$$

For the derivative of the covariance matrix $\mathbf{\Gamma}$ we find then

$$\begin{aligned} \frac{d\mathbf{\Gamma}}{d\tau} &= -\frac{d\mathbf{U}_\xi}{d\tau}\Upsilon\mathbf{U}_\xi^T - \mathbf{U}_\xi\Upsilon\frac{d\mathbf{U}_\xi^T}{d\tau} \\ &= -\mathbf{H}^{(mf)} - \mathbf{\Gamma}\mathbf{H}^{(mf)}\mathbf{\Gamma}, \end{aligned} \quad (\text{A25})$$

which is identical to Eq. (8) using $\mathbf{\Gamma}^2 = -\mathbf{1}$.

APPENDIX B: BEST QUADRATIC APPROXIMATION

In this Appendix we will show Eq. (A16), which can be derived using Wick's theorem. In particular, we will derive this formula for an arbitrary Hamiltonian, which is a sum of even products of Majorana operators. By the application

of normal ordering onto a polynomial $\hat{p}(k)$ of order k we understand the sum of normal-ordered monomials $\hat{m}(l)$ of order $l \leq k$, in other words: $\hat{p}(k) := \sum_{l=0}^k \hat{m}(l)$. Therefore, it is sufficient to show the relation (A16) for arbitrary even products of Majorana operators. Without loss of generality we number the Majorana operators from 1, ..., $2n$ with $n \in \mathbb{N}$. Using normal ordering and Wick's theorem we can write the product $\hat{A} = \hat{a}_1\hat{a}_2 \dots \hat{a}_{2n}$ (a monomial of Majorana operators) in the following way:

$$\hat{A} = \langle \text{vac} | \hat{A} | \text{vac} \rangle + \sum_{i < j} (-1)^{i+j+1} \langle \text{vac} | \hat{A}_{i,j} | \text{vac} \rangle : \hat{a}_i \hat{a}_j : + \hat{Q}, \quad (\text{B1})$$

where \hat{Q} collects all normal-ordered monomials, which are at least quartic in the Majorana operators. We furthermore introduced the reduced product $\hat{A}_{i,j}$, which emerges from \hat{A} by removing the operators \hat{a}_i and \hat{a}_j . If we transform the vacuum state using Eq. (A2), this expansion needs to be modified

according to

$$\hat{U}_{\text{GS}}\hat{A}\hat{U}_{\text{GS}}^\dagger = \langle \Psi_{\text{GS}}|\hat{A}|\Psi_{\text{GS}} \rangle + \sum_{i<j} (-1)^{i+j+1} \langle \Psi_{\text{GS}}|\hat{A}_{i,j}|\Psi_{\text{GS}} \rangle : \\ \times \hat{U}_{\text{GS}}\hat{a}_i\hat{a}_j\hat{U}_{\text{GS}}^\dagger : + \tilde{Q}, \quad (\text{B2})$$

where \tilde{Q} collects terms of order four and higher. Denoting $\mathbf{A} = \mathbf{\Gamma}|_{1,2,\dots,2n}$ and using Eq. (5), we can rewrite the above equation and find

$$\hat{a}_1\hat{a}_2 \dots \hat{a}_{2n} = (-i)^n \text{Pf}(\mathbf{A}) + \sum_{i<j} (-i)^{n-1} (-1)^{i+j+1} \text{Pf}(\mathbf{A}_{i,j}) : \\ \times \hat{U}_{\text{GS}}\hat{a}_i\hat{a}_j\hat{U}_{\text{GS}}^\dagger : + \tilde{Q}. \quad (\text{B3})$$

Here, we have introduced the submatrices $\mathbf{A}_{i,j}$, which emerge from \mathbf{A} by canceling the i th and j th rows and columns. Using

$$\frac{\partial \text{Pf}(\mathbf{A})}{\partial \Gamma_{ij}} = \frac{(-1)^{i+j+1}}{2} \text{Pf}(\mathbf{A}_{i,j}), \quad (\text{B4})$$

we obtain the expression

$$\hat{A} = (-i)^n \text{Pf}(\mathbf{A}) + i \sum_{i,j} (-i)^n \frac{\partial \text{Pf}(\mathbf{A})}{\partial \Gamma_{ij}} : \hat{U}_{\text{GS}}\hat{a}_i\hat{a}_j\hat{U}_{\text{GS}}^\dagger : + \tilde{Q} \\ = \langle \Psi_{\text{GS}}|\hat{A}|\Psi_{\text{GS}} \rangle + \frac{i}{4} : \hat{\mathbf{a}}^T \mathbf{U}_\xi^T \mathbf{A}^{(\text{mf})} \mathbf{U}_\xi \mathbf{a} : + \tilde{Q}, \quad (\text{B5})$$

with matrix entries

$$A_{ij}^{(\text{mf})} = 4 \frac{\partial \langle \Psi_{\text{GS}}|\hat{A}|\Psi_{\text{GS}} \rangle}{\partial \Gamma_{ij}}. \quad (\text{B6})$$

We want to remark that Eq. (B4) can also be used to efficiently calculate the derivative Eq. (9) of Eq. (7).

APPENDIX C: COMPARING NUMERICAL RESULTS OF DMRG AND GHF SIMULATIONS

In this Appendix, we present the difference of the numerical results for the energy expectation value (7) and entanglement entropy (11) displayed in Fig. 2. In Fig. 7 we plot how the energy (a) and entanglement entropy (b) obtained from the GHF ZT algorithm relates to the DMRG simulation results (using a maximal bond dimension of $\chi = 200$) in the weak-long-range regime. Note, that unlike the 399 equally space grid used for the GHF simulations, DMRG simulations were performed on a coarse grid of 49 equally distant values of $\theta \in (0, 0.5)$. Similarly, (c) and (d) present the energy and entanglement entropy relations of the GHF versus DMRG results for the strong-long-range regime, however, for both GHF algorithms. As indicated by the appearance of a stripe-like pattern in the entanglement entropy of Fig. 1 for $\alpha \leq 0.5$, the ZT algorithm (hollow markers) displays numerical instabilities close to the critical point, which is why the ITE algorithm (filled markers) is always used in the strong-long-range regime in the main text. Overall we observe excellent agreement of DMRG and GHF in the short-long-range regime, and qualitative agreement between DMRG and GHF in the strong-long-range regime. An overall larger (lower) value of the energy expectation (entanglement entropy) value is observed for the GHF results, most pronounced around the critical point.

-
- [1] M. Tinkham, *Introduction to Superconductivity*, 2nd ed. (Dover Publications, New York, 2004).
- [2] F. D. M. Haldane, *Rev. Mod. Phys.* **89**, 040502 (2017).
- [3] A. Stern, *Ann. Phys.* **323**, 204 (2008).
- [4] S. Sachdev, *Quantum Phase Transitions*, 2nd ed. (Cambridge University Press, Cambridge, 2011).
- [5] R. J. Elliott, P. Pfeuty, and C. Wood, *Phys. Rev. Lett.* **25**, 443 (1970).
- [6] T. Koffel, M. Lewenstein, and L. Tagliacozzo, *Phys. Rev. Lett.* **109**, 267203 (2012).
- [7] M. Knap, A. Kantian, T. Giamarchi, I. Bloch, M. D. Lukin, and E. Demler, *Phys. Rev. Lett.* **111**, 147205 (2013).
- [8] D. Vodola, L. Lepori, E. Ercolessi, and G. Pupillo, *New J. Phys.* **18**, 015001 (2015).
- [9] S. Fey and K. P. Schmidt, *Phys. Rev. B* **94**, 075156 (2016).
- [10] S. Fey, S. C. Kapfer, and K. P. Schmidt, *Phys. Rev. Lett.* **122**, 017203 (2019).
- [11] J. W. Britton, B. C. Sawyer, A. C. Keith, C.-C. J. Wang, J. K. Freericks, H. Uys, M. J. Biercuk, and J. J. Bollinger, *Nature (London)* **484**, 489 (2012).
- [12] C. Schneider, D. Porras, and T. Schaetz, *Rep. Prog. Phys.* **75**, 024401 (2012).
- [13] A. Friedenauer, H. Schmitz, J. T. Glueckert, D. Porras, and T. Schaetz, *Nat. Phys.* **4**, 757 (2008).
- [14] P. Jurcevic, B. P. Lanyon, P. Hauke, C. Hempel, P. Zoller, R. Blatt, and C. F. Roos, *Nature (London)* **511**, 202 (2014).
- [15] A. Bermudez, T. Schaetz, and M. B. Plenio, *Phys. Rev. Lett.* **110**, 110502 (2013).
- [16] S. Humeniuk, *Phys. Rev. B* **93**, 104412 (2016).
- [17] J. A. Koziol, A. Langheld, S. C. Kapfer, and K. P. Schmidt, *Phys. Rev. B* **103**, 245135 (2021).
- [18] N. Laflorencie, I. Affleck, and M. Berciu, *J. Stat. Mech.: Theory Exp.* (2005) P12001.
- [19] A. W. Sandvik, *Phys. Rev. Lett.* **104**, 137204 (2010).
- [20] V. Bach, E. H. Lieb, and J. P. Solovej, *J. Stat. Phys.* **76**, 3 (1994).
- [21] M. Wimmer, *ACM Trans. Math. Softw.* **38**, 1 (2012).
- [22] S. Bravyi, *Quantum Info. Comput.* **5**, 216 (2005).
- [23] C. V. Kraus and J. I. Cirac, *New J. Phys.* **12**, 113004 (2010).
- [24] T. Shi, E. Demler, and J. Ignacio Cirac, *Ann. Phys.* **390**, 245 (2018).
- [25] P. Jordan and E. Wigner, *Z. Physik* **47**, 631 (1928).
- [26] A. Campa, T. Dauxois, and S. Ruffo, *Phys. Rep.* **480**, 57 (2009).
- [27] N. Defenu, A. Trombettoni, and A. Codello, *Phys. Rev. E* **92**, 052113 (2015).
- [28] M. E. Fisher, S.-k. Ma, and B. G. Nickel, *Phys. Rev. Lett.* **29**, 917 (1972).
- [29] G. C. Wick, *Phys. Rev.* **80**, 268 (1950).
- [30] J. Surace and L. Tagliacozzo, *SciPost Phys. Lect. Notes*, 54 (2022).
- [31] A. Meiburg and B. Bauer, *Phys. Rev. Res.* **4**, 023128 (2022).

- [32] M. Ganahl, J. Beall, M. Hauru, A. G. M. Lewis, T. Wojno, J. H. Yoo, Y. Zou, and G. Vidal, *PRX Quantum* **4**, 010317 (2023).
- [33] L. Amico, R. Fazio, A. Osterloh, and V. Vedral, *Rev. Mod. Phys.* **80**, 517 (2008).
- [34] R. Horodecki, P. Horodecki, M. Horodecki, and K. Horodecki, *Rev. Mod. Phys.* **81**, 865 (2009).
- [35] I. Peschel, *J. Phys. A: Math. Gen.* **36**, L205 (2003).
- [36] G. Vidal, J. I. Latorre, E. Rico, and A. Kitaev, *Phys. Rev. Lett.* **90**, 227902 (2003).
- [37] J. Eisert, M. Cramer, and M. B. Plenio, *Rev. Mod. Phys.* **82**, 277 (2010).
- [38] P. Calabrese and J. Cardy, *J. Stat. Mech.* (2004) P06002.
- [39] B.-Q. Jin and V. E. Korepin, *J. Stat. Phys.* **116**, 79 (2004).
- [40] A. R. Its, B.-Q. Jin, and V. E. Korepin, *J. Phys. A: Math. Gen.* **38**, 2975 (2005).
- [41] J. P. Keating and F. Mezzadri, *Phys. Rev. Lett.* **94**, 050501 (2005).
- [42] J. Eisert and T. J. Osborne, *Phys. Rev. Lett.* **97**, 150404 (2006).
- [43] D. Peter, S. Müller, S. Wessel, and H. P. Büchler, *Phys. Rev. Lett.* **109**, 025303 (2012).
- [44] D. Vodola, L. Lepori, E. Ercolessi, A. V. Gorshkov, and G. Pupillo, *Phys. Rev. Lett.* **113**, 156402 (2014).
- [45] F. Ares, J. G. Esteve, F. Falceto, and A. R. de Queiroz, *Phys. Rev. A* **92**, 042334 (2015).
- [46] F. Iglói and Y.-C. Lin, *J. Stat. Mech.* (2008) P06004.
- [47] S. Nishimoto, *Phys. Rev. B* **84**, 195108 (2011).
- [48] J. Schachenmayer, B. P. Lanyon, C. F. Roos, and A. J. Daley, *Phys. Rev. X* **3**, 031015 (2013).
- [49] M. Ishikawa and M. Wakayama, *Linear and Multilinear Algebra* **39**, 285 (1995).
- [50] M. Ishikawa, M. Wakayama, in *Combinatorial Methods in Representation Theory* (Mathematical Society of Japan, 2000), pp. 133–142.
- [51] M. Ishikawa and M. Wakayama, *J. Comb. Theory, Ser. A* **113**, 113 (2006).
- [52] S. B. Bravyi and A. Y. Kitaev, *Ann. Phys.* **298**, 210 (2002).
- [53] A. Tranter, S. Sofia, J. Seeley, M. Kaicher, J. McClean, R. Babbush, P. V. Coveney, F. Mintert, F. Wilhelm, and P. J. Love, *Int. J. Quantum Chem.* **115**, 1431 (2015).
- [54] Z. Jiang, A. Kalev, W. Mruczkiewicz, and H. Neven, *Quantum* **4**, 276 (2020).
- [55] R. M. Wilcox, *J. Math. Phys.* **8**, 962 (1967).